Cross Section Data for Electron Impact Excitation of Xe II

Qiu-Yao Cao(曹秋瑶)[1], Yu Zhao(赵宇)[1], Xi-Ming Zhu(朱悉铭)[1 2], and Yang Wang(王旸)[1*]

[1]School of Physics,

Harbin Institute of technology, Harbin 150001, China

[2]Key Laboratory of Space Metrology Technology,

State Administration for Market Regulation, Beijing 100094, China

2026/9/1

Abstract

To meet the demands of spectral analysis and collisional-radiative modeling for the Xe plasma, an extensive theoretical calculation of the electron impact excitation of singly-ionized xenon (Xe II) has been carried out. We employed the fully relativistic Dirac *B*-spline *R*-matrix (DBSR) method to deal with the complicated open $5p$-shell structure of Xe II and the subsequent electron scattering problem. A total of 67 low-lying fine-structure levels of $5s^25p^5$, $5s5p^6$, $5p^46s$, $5p^45d$, $5p^46p$ and $5p^47s$ configurations were included in the close-coupling expansion. Following our previous study [Plasma Sources Sci. Technol. 28 105004 (2019)], we modestly refined the configuration-interaction (CI) expansions of the target model to improve both the agreement between the calculated fine-structure level positions and the NIST values, and the convergence of the radiative transition parameters. Comprehensive sets of cross sections for the electron impact excitations between those levels were reported, including the updated integral cross sections for incident energies from threshold to 100 eV, as well as the newly added differential cross sections between 20 and 30 eV. Subsequently, effective collision strengths were derived using a Maxwellian distribution over a broad temperature range from 10^2 to 10^6 K. Radiative transition parameters were also provided for all possible electric dipole-allowed transitions between the target levels. The consistency of the radiative transition parameters is observed between the length-form and the velocity-form, and the convergences with respect to the CI expansions, the target states, and the partial-wave expansions were carefully tested. Comparison with data from other works shows agreement. The present calculations addressed the scarcity of radiative and electron-collisional data for Xe II, and the full datasets are openly available in the Science Data Bank.

Keywords: cross sections, Xe II, electron impact excitation, Dirac *B*-spline *R*-matrix, effective collision strength

PACS: 34.50.Fa, 31.15.am, 34.10.+x

1. Introduction

Xenon gas has been widely used in the area of electric propulsion systems over the past several decades, because of its advantages such as nontoxicity[1–3], chemical inertness, and a low ionization threshold. It is also important in fusion research[4] and is related to astrophysics when studying stellar atmospheres[5,6]. These low-temperature

*Corresponding author. E-mail: yangwang0624@foxmail.com

plasma environments produce a great number of neutral atomic xenon (Xe I) atoms and singly-ionized xenon (Xe II) ions. Many spectra of Xe I and Xe II can be observed, and they are usually used for the plasma modeling[7,8] to obtain electron temperatures, electron densities, and other plasma parameters. Therefore, accurate and comprehensive atomic data sets, such as oscillator strengths, electron impact cross sections and effective collision strengths for Xe and its ions are essential for developing a reliable collisional-radiative model, which in turn enables the extraction of detailed plasma parameters. More detailed collisional data are also required. For example, differential cross sections (DCS) directly characterize the probability distribution of collision processes as functions of both incident electron energy and scattering angle[9]. These data provide essential information for understanding interactions between heavy atoms or ions and electrons.

For Xe I, detailed experimental and theoretical studies have been reported[10–12]. In contrast, studies on Xe II remain comparatively limited, due to experimental challenges in preparing and purifying Xe II ions in the laboratory, as well as the computational complexities arising from strong configuration interactions. In 1994, Gigosos et al. measured Stark widths and shifts, as well as transition probabilities of Xe II in a pulsed arc plasma source[13]. In 2000, Rocco et al. used a Laser Produced Plasma (LPP) spectroscopic source to measure Xe II transition probabilities of 18 $6p$-$6d$ processes[14]. In 2002, Zielinska et al. measured Branching ratios for Xe II electric dipole transitions in the range from 200 nm to 2400 nm, using a high-current hollow cathode lamp operated with pure Xe gas[15]. In 2011, Yüce et al. measured the equivalent widths of clean and unblended Xe II absorption lines in the high-resolution Ultraviolet and Visual Echelle Spectrograph spectra in four slowly rotating mercury-manganese (HgMn) stars. Then within the framework of Local Thermodynamic Equilibrium, they used ATLAS model atmospheres together with the WIDTH curve-of-growth code to derive the revised wavelengths of Xe II lines, the astrophysical oscillator strengths, and the xenon abundances in the stellar atmospheres[5]. In 2014, Sayres et al. used the core–hole absorption spectroscopy to measure the alignment prepared through the strong-field Xe II[16]. In 2021, Fushitani et al. employed ultrafast photoelectron spectroscopy of the Rydberg states of Xe II lying above the doubleionization threshold by using EUV-FEL and NIR laser pulses, and obtained the lifetimes, the photoelectron peaks and the quantum defects of autoionizing Rydberg states of Xe II[17]. In contrast to structural investigations, systematic studies on the electron impact excitation cross sections of Xe II remain relatively scarce.

The challenges in calculating cross sections for electron collisions with Xe II originate from its complicated ionic target. As a heavy ion, Xe II exhibits a pronounced term dependence for its open $5p^4nl$ outer-shell configurations as well as strong spin-orbit interaction effects, which result in a very rich and dense target structure and substantial fine-structure splittings. Inner-core and core-valence correlation and relaxation effects also play a critical role, particularly for transitions originating from the ground state. These complexities present considerable challenges to all theoretical approaches, especially to those relying on orthogonal bases of one-electron orbitals. Therefore, a fully relativistic treatment is required for accurate modeling of Xe II. Two dominant calculation frameworks, the distorted-wave method based on the perturbation theory[18], and the R-matrix method based on the partial-wave and close-coupling theories[19], are usually used to solve this type of problem. Gupta et al.[20] used the relativistic distorted-wave (RDW) method in 2018 to calculate the electron impact excitation cross sections from the ground state. Shortly thereafter in 2019, Wang et al.[21] presented a nonperturbative treatment using the fully relativistic

Dirac B-spline R-matrix (DBSR) method to construct a target model of 67 low-lying fine-structure levels. Within this model, the multi-electron Dirac-Coulomb Hamiltonian was applied to comprehensively account for valence and core-valence correlations as well as relativistic effects for this heavy ion. Accurate radiative and collisional parameters were obtained and successfully applied to xenon collisional-radiative models in electric propulsion studies[22,23]. Motivated by the data needs for collisional-radiative plasma modeling, the present work aims to provide an extended dataset for Xe II based on our previous study in 2019[21]. We made a modest extension to the configuration-interaction (CI) expansion of the target wavefunctions, to further improve the convergence and accuracy of the structure calculations. On this basis, a full set of radiative parameters, including line strengths, transition probabilities, and oscillator strengths for all 701 electric dipole-allowed transitions in the Xe II model are calculated, and we classified the oscillator strengths according to the relative differences between length-form and velocity-form values. We updated the excitation cross sections, and added differential cross sections and effective collision strengths of electron impact excitations between the 67 states in the Xe II model. The complete datasets are openly accessible in the Science Data Bank to facilitate their use in spectroscopic analysis and plasma modeling.

The paper is organized as follows. In Section 2, the numerical approaches applied to the structure and scattering calculations are briefly introduced. This section also demonstrates the convergence of CI expansions and gives the relative differences of the oscillator strengths between the length-form and the velocity-form. In Section 3, the convergences with respect to the target states and partial-wave expansions are tested. Then, we discuss the calculated integral and differential cross sections and effective collision strengths for electron impact excitations of Xe II and also give a comparison between the data presented in this work and those from the previous work, to validate the reliability of our data. Finally, the conclusions are given in Section 4.

2. Calculation Details

We performed the present calculations using the fully relativistic DBSR method[24] which is an extension of the BSR approach[25] to the fully relativistic scheme. Compared to the Breit-Pauli model, it leads to much more numerically extensive calculations due to the larger number of individual B-spline and a larger number of channels in jj-coupling. The Dirac-Coulomb (DC) Hamiltonian was used to describe the N-electron target and the (N+1)-electron collision systems, respectively. In atomic units, the DC Hamiltonian for N electrons in a central field made by the nucleus of charge Z is given by

$$H^{\mathrm{DC}} = \sum_{i=1}^{N} \left(c\alpha \cdot \mathbf{p}_i + \beta c^2 - \frac{Z}{r_i} \right) + \sum_{i>j}^{N} \frac{1}{r_{ij}} \tag{1}$$

where the components of the vector α and β are the Dirac matrices, $\mathbf{p}_i$ is the momentum operator of electron "i", and $c \approx 137$ is the speed of light. For each partial-wave symmetry J^π, with J denoting the total electronic angular momentum in a jj-coupling scheme and π indicating the parity, the total wave function is constructed from Dirac four-component spinors

$$\phi_{n\kappa m} = \frac{1}{r}\begin{pmatrix} P_{n\kappa}(r)\,\chi_{\kappa m}(\vartheta,\varphi) \\ iQ_{n\kappa}(r)\,\chi_{-\kappa m}(\vartheta,\varphi) \end{pmatrix} \tag{2}$$

where χ_{km} is the spinor spherical harmonic, and κ is the relativistic angular momentum quantum number. We expand the radial functions for the large and small components $P(r)$ and $Q(r)$ in separate B-spline bases as

$$P(r) = \sum_{i=1}^{n_p} p_i B_i^{k_p}(r), \qquad Q(r) = \sum_{i=1}^{n_q} q_i B_i^{k_q}(r) \tag{3}$$

where $B_i^{K_p}$ and $B_i^{K_q}$ are the separate B-spline bases; and n_p and n_q are the numbers of B-spline bases used for the expandings of $P(r)$ and $Q(r)$, respectively. Both B-spline bases are defined on the same grid, with the same number of intervals, n_v. Only in this case can the calculations of various matrix elements and integrals of interest be performed with the same routines and at the same level of required computational resources as in the case of a single B-spline basis. The coefficients p_i and q_i are found by diagonalizing the total (N+1)-electron Hamiltonian inside the R-matrix box.

The target states in the present calculations were considered as an open-shell system above a closed [Kr]$4d^{10}$ core. All calculations were completely ab initio, with the multi-channel target states of Xe II represented through B-spline box-based expansions of the form

$$\begin{aligned} \Phi(5s^2 5p^4 nl, J\pi) &= \mathcal{A}\sum_{nl,J\pi}\left[\phi(5s^2 5p^4)P(nl)\right]^{J\pi} + \mathcal{A}\sum_{nl,J\pi}\left[\phi(5s^2 5p^3 5d)P(nl)\right]^{J\pi} \\ &+ \mathcal{A}\sum_{nl,J\pi}\left[\phi(5s5p^5)P(nl)\right]^{J\pi} + a\varphi(5s^2 5p^5) + b\varphi(5s5p^6) \end{aligned} \tag{4}$$

Here J is the total electronic angular momentum of the target state, π is the parity, and all intermediate terms in the expansion were included. $\mathcal{A}$ denotes the anti-symmetrization operator, $P(nl)$ denotes an orbital of the outer valence electron, while the ϕ and φ functions represent the CI expansions of the Xe III and Xe II states, respectively. The CI wave functions were generated from separate Dirac-Fock calculations by employing the relativistic atomic structure packages GRASP2K[26] and DBSR_HF[27]. The core-valence correlation was accounted for through the CI expansions of these states with non-orthogonal orbitals. These expansions included all single and double excitations from the $5s$ and $5p$ orbitals to the $5d$, $5f$, as well as $6l$ and $7l$ (l = 0-3) correlated orbitals. Different sets of correlated orbitals were optimized separately for the lowest state of each $J\pi$ symmetry. To keep the final precise expansions for the target states to a reasonable size, the maximum of the principal quantum number $n_{\max}$in the CI expansions was increased from 5 to 9 due to computational resource demands, and the cut-off parameter was decreased from 0.02 to 0.001 to test the convergence. For each level, we calculated the energy with every $n_{\max}$ and every cut-off parameter, and the ratio to the energy with $n_{\max} = 9$ and the cut-off parameter 0.001 is shown in Figure 1. It is clear that the results for $n_{\max} = 7$ have already converged, and the convergence of the results for the cut-off parameters not larger than 0.01 is good enough. Consequently, $n_{\max}$ was set to 7 and the cut-off parameters were varied in the range from 0.01 to 0.006 for different terms. This range is smaller than the cut-off parameter of 0.01, which is generally

adopted in our previous model[21]. As a result, the CI expansions for some target states are correspondingly finer, which improves both the agreement between the calculated fine-structure level positions and the NIST values and the convergence of the radiative transition parameters.

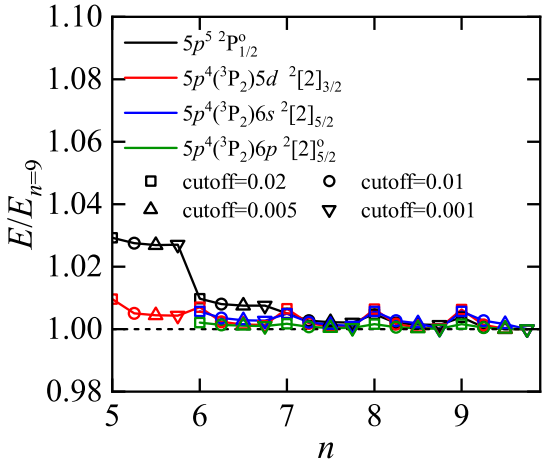


Figure 1: Convergence of select states with $n_{\max}$ increasing from 5 to 9, and the cut-off parameter decreasing from 0.02 to 0.001 for each $n_{\max}$.

The resulting CI expansions with sizes between 400 and 800 for each target state were manageable for the subsequent scattering calculation with currently available computational resources. It is not possible to construct all the states with currently available computer programs when considering the time-consuming of the following scattering calculation. Hence, in the present calculation, we selected the most important states of $5s^25p^5$, $5s5p^6$, $5s^25p^46s$, $5s^25p^45d$ and $5s^25p^46p$ configurations with consideration of their strong term dependence of the orbitals and configuration mixing. This would also allow us to describe well the most important electric dipole-allowed transitions between orbitals $5p$, $5d$, $6s$ and $6p$. The present theoretical target model has been proven to provide sufficient accuracy for its application to xenon collisional-radiative models in electric propulsion systems[22,23]. Building upon our previous work, a comprehensive set of radiative parameters for all 701 electric dipole-allowed transitions between the considered target states is provided. A representative subset of oscillator strengths is presented along with available data from the NIST database[28] and Yüce et al.[5] in Table 1. The two published sets of data above are limited, but we observe good agreement between our DBSR results and the data reported by NIST as well as by Yüce et al. in Table 1, which satisfies the precision criteria adopted for the current target model. Considering the agreement between the length-form(Babushkin form, f_L) and the velocity-form(Coulomb form, f_V) of oscillator strengths to some extent indicates the accuracy of wavefunctions and convergence of CI expansions, we calculated the relative difference $\Delta f = (f_V - f_L)/\max(f_L, f_V)$ between f_L and f_V of the present target model. According to NIST ASD[28], the relative differences can be classified into four grades: A ($\leq$ 3%), B ($\leq$ 10%), C ($\leq$ 25%) and D ($\leq$ 50%), which are shown in Figure 2. It is clear that about 80% results for all the 701 electric dipole-allowed transitions are within 25%, which indicates good agreement between f_L and f_V. It provides some confidence for the target description. The complete dataset of line strengths(S), transition probabilities(A), oscillator strengths(f), as well as the classifications of the relative difference, are available in Science Data Bank.

Table 1: Line strengths(S), transition probabilities(A) and oscillator strengths(f) of DBSR calculations for selected electric dipole (E1) lines of Xe II.

Lower level	Upper level	λ(nm)	S_{ij}	A_{ij} (s^{-1})	f_{ij}	f_{exp} [5]	f_{NIST} [28]
$5p^5\ ^2P^o_{3/2}$	$5s5p^6\ ^2S_{1/2}$	108.843	1.16E-01	9.11E+07	8.09E-03		
	$5p^4\ (^3P_2)\ 6s\ ^2[2]_{5/2}$	105.326	1.65E-01	5.21E+07	1.23E-02		
	$5p^4\ (^3P_2)\ 6s\ ^2[2]_{3/2}$	103.076	1.61E+00	8.14E+08	1.22E-01		
	$5p^4\ (^3P_2)\ 5d\ ^2[2]_{5/2}$	102.396	7.84E-02	2.77E+07	6.04E-03		
	$5p^4\ (^3P_2)\ 5d\ ^2[2]_{3/2}$	101.553	7.97E-02	4.32E+07	6.19E-03		
	$5p^4\ (^3P_2)\ 5d\ ^2[1]_{1/2}$	101.083	1.15E-02	1.27E+07	8.99E-04		
	$5p^4\ (^3P_0)\ 6s\ ^2[0]_{1/2}$	96.715	3.01E-01	3.60E+08	2.42E-02		
$5p^5\ ^2P^o_{1/2}$	$5s5p^6\ ^2S_{1/2}$	122.717	1.24E-01	6.78E+07	1.53E-02		
	$5p^4\ (^3P_2)\ 6s\ ^2[2]_{3/2}$	115.435	4.63E-02	1.69E+07	6.30E-03		
	$5p^4\ (^3P_2)\ 5d\ ^2[2]_{3/2}$	113.529	1.15E-02	4.52E+06	1.60E-03		
	$5p^4\ (^3P_2)\ 5d\ ^2[1]_{1/2}$	112.941	1.85E-02	1.48E+07	2.60E-03		
	$5p^4\ (^3P_0)\ 6s\ ^2[0]_{1/2}$	107.516	5.62E-03	4.92E+06	8.13E-04		
	$5p^4\ (^3P_1)\ 6s\ ^2[1]_{3/2}$	105.648	8.60E-02	4.00E+07	1.27E-02		
	$5p^4\ (^3P_1)\ 6s\ ^2[1]_{1/2}$	101.243	4.58E-01	4.51E+08	6.89E-02		
$5s5p^6\ ^2S_{1/2}$	$5p^4\ (^3P_2)\ 6p\ ^2[2]^o_{3/2}$	470.650	1.37E-01	8.22E+05	4.75E-03		
	$5p^4\ (^3P_2)\ 6p\ ^2[1]^o_{1/2}$	439.824	9.83E-02	1.45E+06	3.64E-03	5.61E-03	
	$5p^4\ (^3P_2)\ 6p\ ^2[1]^o_{3/2}$	379.540	2.40E-01	2.56E+06	1.01E-02		
	$5p^4\ (^3P_0)\ 6p\ ^2[1]^o_{1/2}$	333.989	5.95E-02	1.85E+06	2.83E-03		
	$5p^4\ (^3P_1)\ 6p\ ^2[0]^o_{1/2}$	326.333	8.21E-03	2.71E+05	3.98E-04		
	$5p^4\ (^3P_0)\ 6p\ ^2[1]^o_{3/2}$	323.994	1.07E-01	1.85E+06	5.29E-03		
	$5p^4\ (^3P_1)\ 6p\ ^2[2]^o_{3/2}$	304.981	1.77E-02	3.53E+05	9.13E-04		
$5p^4\ (^3P_2)\ 6s\ ^2[2]_{5/2}$	$5p^4\ (^3P_2)\ 6p\ ^2[2]^o_{3/2}$	550.092	2.24E+01	5.48E+07	1.91E-01	1.42E-01	
	$5p^4\ (^3P_2)\ 6p\ ^2[2]^o_{5/2}$	548.738	4.69E+01	7.74E+07	4.03E-01	4.70E-01	3.7E-01
	$5p^4\ (^3P_2)\ 6p\ ^2[3]^o_{5/2}$	510.051	1.21E+00	2.58E+06	1.13E-02	1.05E-02	
	$5p^4\ (^3P_2)\ 6p\ ^2[3]^o_{7/2}$	504.119	5.49E+01	8.87E+07	5.16E-01	6.64E-01	5.2E-01
	$5p^4\ (^3P_2)\ 6p\ ^2[1]^o_{3/2}$	429.567	3.39E+00	1.77E+07	3.73E-02	1.49E-02	
	$5p^4\ (^3P_0)\ 6p\ ^2[1]^o_{3/2}$	359.759	2.36E-01	2.23E+06	3.17E-03		
	$5p^4\ (^3P_1)\ 6p\ ^2[2]^o_{5/2}$	344.327	8.88E-02	6.52E+05	1.26E-03		
$5p^4\ (^3P_2)\ 6s\ ^2[2]_{3/2}$	$5p^4\ (^3P_2)\ 6p\ ^2[2]^o_{3/2}$	620.864	8.03E+00	1.27E+07	8.92E-02	1.12E-01	1.5E-01
	$5p^4\ (^3P_2)\ 6p\ ^2[2]^o_{5/2}$	619.140	2.66E-01	2.84E+05	2.97E-03		
	$5p^4\ (^3P_2)\ 6p\ ^2[3]^o_{5/2}$	570.331	4.43E+01	6.39E+07	5.46E-01	5.60E-01	4.1E-01
	$5p^4\ (^3P_2)\ 6p\ ^2[1]^o_{1/2}$	568.319	1.50E+01	6.54E+07	1.86E-01	1.99E-01	1.5E-01
	$5p^4\ (^3P_2)\ 6p\ ^2[1]^o_{3/2}$	471.541	1.95E+01	7.28E+07	2.88E-01		2.6E-01
	$5p^4\ (^3P_0)\ 6p\ ^2[1]^o_{1/2}$	403.218	2.73E-01	3.44E+06	4.81E-03		
	$5p^4\ (^3P_0)\ 6p\ ^2[1]^o_{3/2}$	388.739	6.66E-02	4.82E+05	1.23E-03		

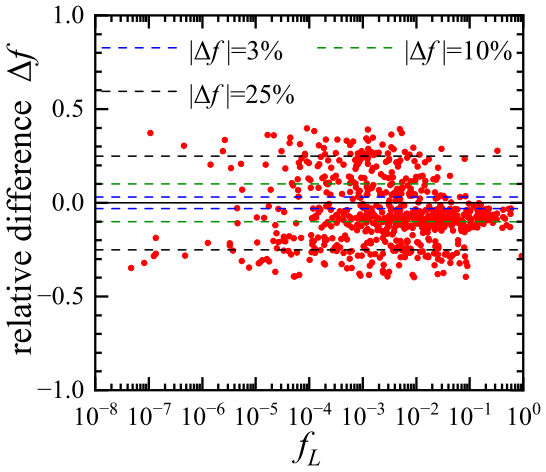


Figure 2: The relative differences between f_L and f_V.

We set the radius of the internal spherical R-matrix region to $50\,a_0$, where $a_0 = 0.529 \times 10^{-10}$ m is the Bohr radius. This choice allowed us to obtain a sufficiently good description for the low-lying bound states of the configurations mentioned above. We employed 128 B-splines of orders 8 and 9 for the large and small components of the spinors, respectively. The different B-spline orders for the two components ensure the absence of spurious solutions[29]. The relatively large number of splines was used because we employed a finite-size nuclear model with a Fermi potential[30].

The present scattering model included 67 fine-structure levels of the Xe II $5s^25p^5$, $5s5p^6$, $5p^46s$, $5p^45d$, $5p^46p$, and $5p^47s$ configurations. This model will be labeled DBSR-67 in the following discussion. We adjusted the excitation energies to the NIST values in the subsequent collision calculation. (N+1)-electron "bound-bound" terms do not have to be included in the close-coupling expansion of the collision problem since we do not force orthogonality between the target and the projectile orbitals. As a result, using the experimental thresholds does not carry the danger of otherwise possible inconsistencies in the relative positions of the N-electron target and the (N+1)-electron resonance states. Therefore, the effect of this correction is generally small, especially on the rate coefficients to be calculated from the cross sections. However, it is beneficial in making a direct comparison with experiment possible. The scattering calculations included up to 306 coupled scattering channels, and interaction matrices with dimensions of up to about 50,000 needed to be diagonalized for each partial wave. Partial-wave contributions up to $2J = 50$ were calculated explicitly, which was sufficient to obtain converged results for all transitions considered in the present theoretical model. We employed a parallelized version of the DBSR codes using MPI parallelization and the SCALAPACK libraries[31]. Finally, the scattering amplitudes and corresponding parameters were then found by matching the inner-region solutions at the R-matrix boundary with the asymptotic solutions in the external region. We employed FARM program[32] in the external region to calculate the transition matrix elements, and subsequently obtain the collisions strengths and cross sections using standard formulas[33]. In the resonance region for impact energies below the excitation energy of the highest level included in the close-coupling expansion, we used a fine energy step of 10^{-3} Ry to properly map out the relevant resonance structures. For energies above the highest excitation threshold included in the close-coupling expansion, the collision strengths vary smoothly, and hence we chose

a coarser electron energy step of 10^{-2} Ry. The differential cross sections were calculated by the MJK program of Grum-Grzhimailo[34] from the transition matrix elements produced by the FARM program. The energy-dependent integal excitation cross section can be expressed as

$$\sigma_{ij}(E) = \pi a_0^2 \frac{\Omega_{ij}(E)}{k_i^2 g_i}, \tag{5}$$

where i and j denote the initial and final states of the transition, respectively, and $\Omega_{ij}(E)$ is the collision strength for the $i \rightarrow j$ transition. k_i is the wave number of the colliding electron incident on the target ion in state i, a_0 is the Bohr radius, and $g_i = (2J_i + 1)$ is the statistical weight of the state i.

The effective collision strengths $\Upsilon_{ij}(T_e)$, which are needed for applications in plasma modeling and spectral analysis, were also calculated by convoluting the collision strengths Ω over a Maxwellian distribution for electron temperatures from 10^2 to 10^6 K as follows

$$\Upsilon_{ij}(T_e) = \int_{E_{th}}^{\infty} dE\ \Omega_{ij}(E) \exp\left(-\frac{E - E_{th}}{kT_e}\right) \tag{6}$$

Here T_e is the electron temperature, k is the Boltzmann constant, and E_{th} is the transition energy for the $i \rightarrow j$ transition.

3. Results and Discussions

3.1. Integral Cross Sections and Effective Collision Strengths

In this section, we present the DBSR-67 results for electron impact excitation integral cross sections (ICS) in Xe II, covering electron energies from the threshold up to 100 eV. We first test the convergence with respect to the target states and partial-wave expansions in Figure 3, taking the $5p^5\ ^2\mathrm{P}^{\mathrm{o}}_{3/2}$-$5p^4\ (^3\mathrm{P}_2)\ 6s\ ^2[2]_{5/2}$ transition for example. Panel (a) illustrates how convergence varies alongside the number of target states adopted in the target model. These tested models contain 20, 40, 60, 67 and 76 discrete target states, labeled DBSR-20 up to DBSR-76 respectively. As the number of target states increases from 20 to 60, the cross sections converge rapidly. The difference between DBSR-60 and DBSR-67 is negligible, and DBSR-76, with all target states of DBSR-67 plus nine $6d$ target states (the maximum we can handle with our current computational resources), hardly produces any further changes. It proves the reliability of the DBSR-67 model adopted in this work. Panel (b) shows the convergence with respect to the number of partial waves. As $2J_{\mathrm{max}}$ of the partial wave increases from 20, the cross sections gradually converge. Generally, the calculations become fully converged when $2J_{\mathrm{max}} = 46$, thereby confirming that our final model adopting $2J_{\mathrm{max}} = 50$ is sufficient. The top-up procedure is also considered for the influence of higher partial waves. In panel (b), it can be seen that the contribution of top-up appears only at higher electron energies, and the relative difference of the cross sections between the calculations with and without the top-up procedure is less than 10% below 100 eV. This indicates that the results without the top-up procedure are still reliable.

The ICSs for selected transitions together with the corresponding Maxwellian-averaged effective collision strengths (ECS) are illustrated in Figures 4 and 5. Figure 4 shows the present DBSR-67 results for integral cross

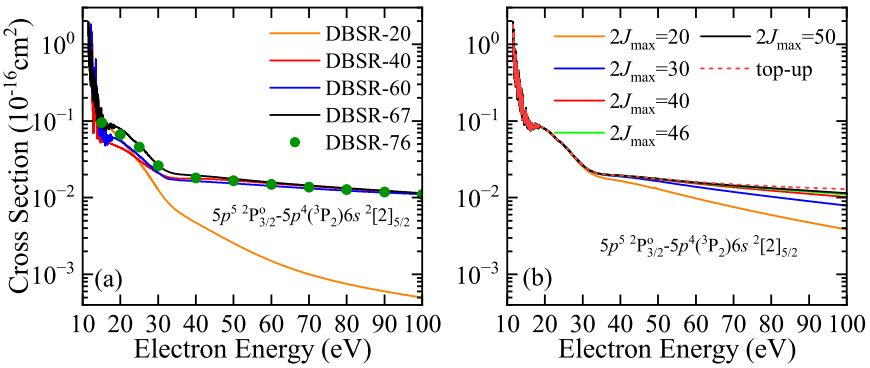


Figure 3: The convergence tests with respect to the target states and partial-wave expansions.

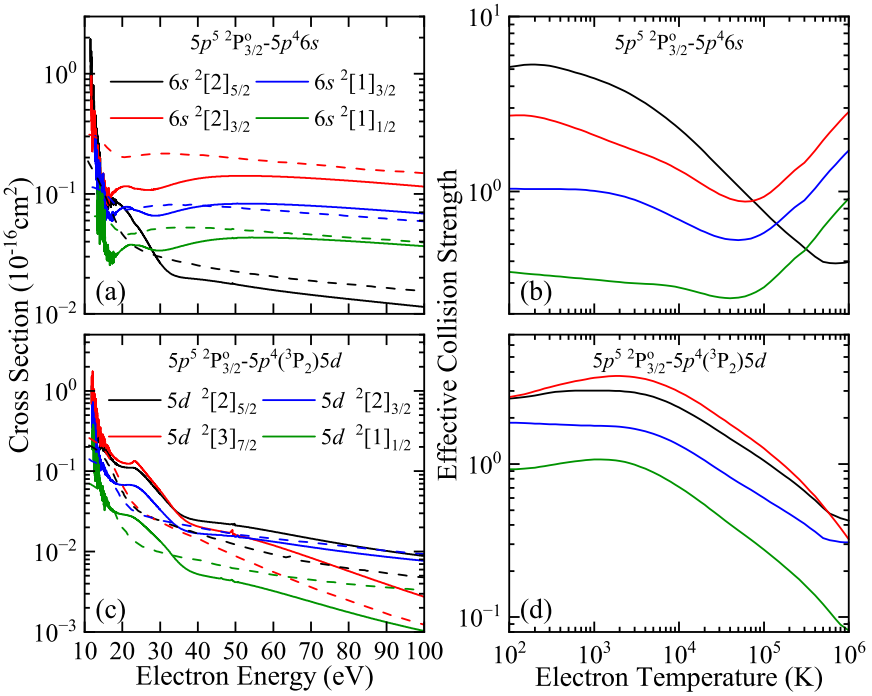


Figure 4: electron impact excitation integral cross sections and effective collision strengths of Xe II for fine-structure transitions from the ground state $5p^5\ ^2P^o_{3/2}$ to selected $5p^4 6s$ and $5p^4 5d$ levels. Solid lines represent the results of the present work, and dashed lines with the same color denote the corresponding RDW[20] results.

sections and effective collision strengths from the ground state (gs) $5p^5\ ^2\mathrm{P}^{\mathrm{o}}_{3/2}$ to selected $5p^4 6s$ and $5p^4\left(^3\mathrm{P}_2\right)5d$ states. Panels (a) and (c) reveal pronounced resonance structures in the energy dependence of ICS in the low-energy region up to 20 eV. Such resonant behavior is a characteristic feature of electron-ion collision processes and will play a pivotal role in determining the thermally averaged collision strengths at low temperatures. Additionally, a minor peak is generally observed at energies around 25 eV, which appears to be a common pattern for excitation cross sections from the ground state of Xe II. The comparison has been made between the present DBSR results and the only available theoretical calculations on the e-Xe II case by the RDW method of Gupta et al [20]. The curve shapes of DBSR and RDW are generally consistent, and differences exist only in resonance structures and ICS values. To quantify this comparison, we calculated the relative deviation between the present DBSR and the RDW cross sections, averaged over the four fine-structure transitions from the ground state to each of the $5p^4 6s$ and $5p^4\left(^3\mathrm{P}_2\right)5d$ manifolds, at four representative energies. For the gs-$6s$ transitions, the average deviation is 28%, 39%, 31%, and 18% at 20, 30, 50, and 100 eV, respectively. The local maximum at 30 eV coincides with the minor secondary peak near 25 eV noted above for excitation from the ground state, a channel-coupling feature that is absent from the perturbative RDW treatment, and the deviation falls to its lowest value by 100 eV. For the gs-$5d$ transitions, the corresponding averages are 42%, 42%, 31%, and 46%, so the deviation instead falls to a minimum near 50 eV before rising again at 100 eV. This is likely related, at least in part, to the comparatively small magnitude of the $5d$ cross sections at higher energies, where a modest absolute difference between the two calculations translates into a disproportionately large relative deviation. The comparison therefore indicates that, while the discrepancy between DBSR and RDW narrows substantially with increasing energy for some transitions, it does not vanish uniformly by 100 eV and can remain appreciable for transitions with intrinsically small cross sections. The corresponding ECS for these transitions, displayed in Figures 4(b) and (d), exhibit distinct temperature-dependent behaviors. In general, the relative magnitudes of ECS for different transitions can vary significantly, reflecting differences in transition probabilities and coupling strengths between the initial and final states. For instance, as shown in panel (b) for gs-$6s$ transitions, the ECS values decrease in the order from $6s\ ^2[2]_{5/2}$ to $6s\ ^2[1]_{1/2}$ at temperatures below 10^5 K, consistent with the ordering of the ICS curves in panel (a) at low energies (<20 eV). Notably, the ECS curve of $6s\ ^2[2]_{5/2}$ level becomes lowest at temperatures close to 10^6 K, corresponding to its ICS becoming smallest at higher incident energies. This behavior also shifts the minimum of its ECS curve toward higher temperatures compared to the other three gs-$6s$ transitions. Similar trends can be seen for gs-$5d$ transitions in panels (c) and (d). Their ECS curves remain relatively flat at temperatures below 2×10^4 K, after which they decrease gradually with increasing temperature.

As common upper levels in the spectra of the Xe II plasma, the $5p^4\left(^3\mathrm{P}_2\right)6p$ states are important. ICS and ECS to selected $5p^4\left(^3\mathrm{P}_2\right)6p$ states from gs, $5p^4\left(^3\mathrm{P}_2\right)6s\ ^2[2]_{5/2}$ and $5p^4\left(^3\mathrm{P}_2\right)5d\ ^2[2]_{5/2}$ by DBSR are shown in Figure 5. It is clear that there are obvious differences of the curve shapes of ICS and ECS between selected gs-$6p$ and $6s$, $5d$-$6p$ transitions. The gs-$6p$ transitions in panel (a) reveals pronounced resonance structures in the energy dependence of ICS in the low-energy region up to 20 eV, but the resonances are weaker than those of the gs-$6s$ and $5d$ transitions shown in Figure 4. Additionally, a minor peak is generally observed at energies around 23 eV for these transitions, consistent with the behavior shown in Figure 4. Their corresponding ECS, shown in panel (b), decrease

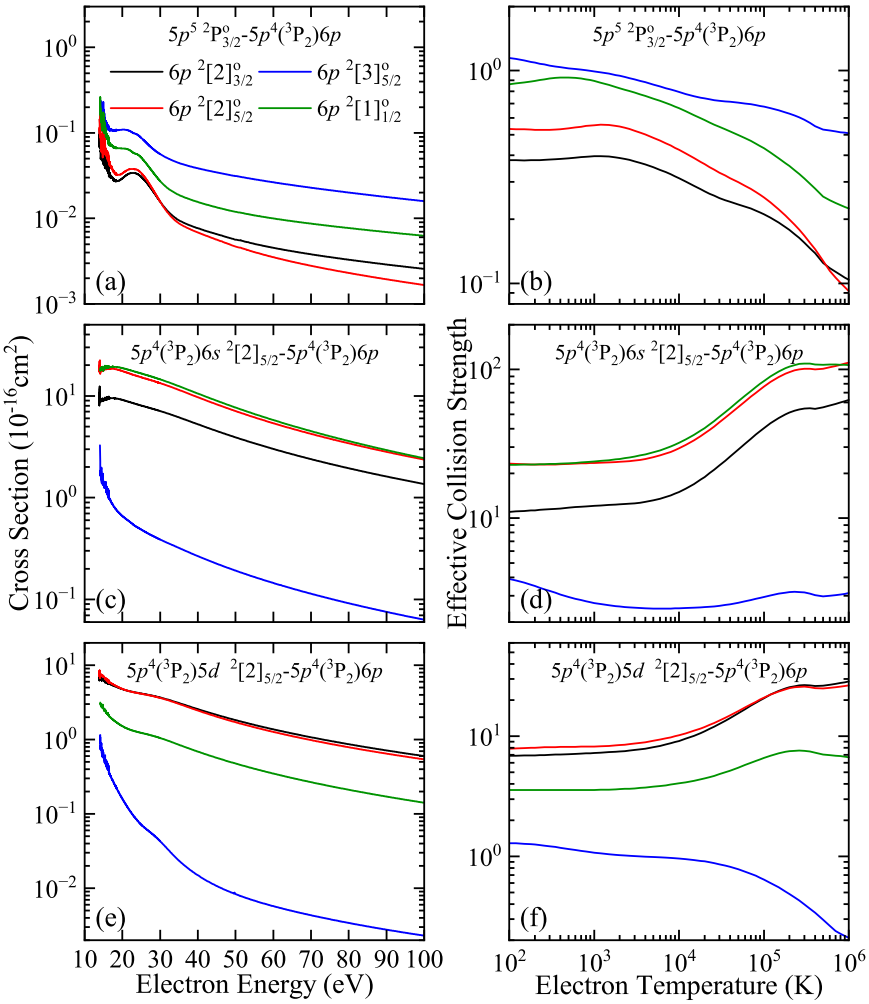


Figure 5: electron impact excitation integral cross sections and effective collision strengths of Xe II for fine-structure transitions from $5p^5\ ^2P^o_{3/2}$, $5p^4\ (^3P_2)\ 6s\ ^2[2]_{5/2}$ and $5p^4\ (^3P_2)\ 5d\ ^2[2]_{5/2}$ to selected $5p^4\ (^3P_2)\ 6p$ levels.

with increasing electron temperature, exhibiting a trend analogous to that presented in Figure 4 (d). For the $6s$, $5d$-$6p$ transitions in panels (c) and (e), their ICS have larger magnitudes and smaller resonance structures than those of the gs-$6p$ transitions. The ICS curves of the transitions from $6s\ ^2[2]_{5/2}$ and $5d\ ^2[2]_{5/2}$ to $6p\ ^2[2]^o_{3/2}$, $6p\ ^2[2]^o_{5/2}$ and $6p\ ^2[1]^o_{1/2}$ exhibit similar shapes. They are nearly linear, maintaining essentially identical slopes for incident energies above 20 eV. Especially, the curves of transitions from $5p^4\ (^3P_2)\ 6s\ ^2[2]_{5/2}$ to $6p\ ^2[2]^o_{5/2}$ and $6p\ ^2[1]^o_{1/2}$ nearly overlap, and so do the curves of $5d\ ^2[2]_{5/2}$-$6p\ ^2[2]^o_{3/2}$ and $6p\ ^2[2]^o_{5/2}$. Similarities also appear in the shapes of ECS curves of the six transitions mentioned above, as depicted in panels (d) and (f). In general, these ECS values increase with rising temperature. The curves exhibit steep slopes between 10^4 and 2×10^5 K, followed by a gradual decline up to 5×10^5 K. At temperatures exceeding 5×10^5 K, the ECS of the transitions to $6p\ ^2[2]^o_{3/2}$ and $6p\ ^2[2]^o_{5/2}$ increases, whereas those for the transitions to $6p\ ^2[1]^o_{1/2}$ continue to decrease. Notably, the ICS of the transitions from $6s\ ^2[2]_{5/2}$ and $5d\ ^2[2]_{5/2}$ to $6p\ ^2[3]^o_{5/2}$ exhibit smaller magnitudes compared to those of the transitions discussed above. They decrease rapidly at low temperatures but gradually decrease slowly until the temperature approaches 10^6 K. Their corresponding ECS also exhibit smaller magnitudes and decrease as the electron temperature increases to 10^4 K. However, beyond 10^4 K, the ECS of $6s\ ^2[2]_{5/2}$-$6p\ ^2[3]^o_{5/2}$ increases as the temperature increases, behaving similarly to $6s\ ^2[2]_{5/2}$-$6p\ ^2[2]^o_{5/2}$, whereas the ECS of $5d\ ^2[2]_{5/2}$-$6p\ ^2[3]^o_{5/2}$ continues to decrease.

The thermally averaged ECS are essential for emission-line modeling across various plasma environments. Partial results of present calculations for fine-structure transitions from ground state are listed in Table 2, covering ten selected temperature points ranging from 10^2 to 10^6 K. A table of complete ECS and files of complete ICS datasets for transitions between all fine-structure levels of present DBSR-67 model are openly accessible in the Science Data Bank. To provide users with practical guidance on data reliability, we note that rigorous, statistically defined uncertainty propagation is generally not feasible for a close-coupling calculation of the present complexity. Following the general framework proposed by Chung et al.[35] for assessing the uncertainty of theoretical atomic and molecular data, we instead build confidence in the reported cross sections through a combination of internal consistency indicators. First, the level of agreement between the length-form and velocity-form of oscillator strengths discussed above offers a useful, if indirect, indicator of the quality of the target wavefunctions underlying both the radiative and collisional calculations. Second, the convergence tests with respect to the target states and partial-wave expansions in Figure3 demonstrate the numerical stability of the present model. Third, since no direct experimental cross-section measurements are currently available for Xe II, we compare the present results with the independent RDW calculations. The general consistency in curve shape between the two independently constructed methods provides a further complementary indicator of reliability. Finally, the present cross sections, when applied within collisional-radiative models of xenon electric-propulsion plasmas, have shown good agreement with experimental plasma diagnostics[22,23], offering the closest available indirect connection to experiment for this system. Taken together, these internal consistency checks support the reliability of the present scattering data despite this continued absence of direct experimental benchmarks for Xe II.

Table 2: Effective collision strengths for fine-structure transitions from the ground state $5p^5\ {}^2\mathrm{P}^{\mathrm{o}}_{3/2}$ in Xe II

Upper level	$T \times 10^4$ K									
	0.1	0.2	0.5	1	2	5	10	20	50	100
$5p^5\ {}^2\mathrm{P}^{\mathrm{o}}_{1/2}$	2.588E+00	2.574E+00	2.539E+00	2.496E+00	2.473E+00	2.578E+00	2.506E+00	2.181E+00	1.579E+00	1.278E+00
$5s5p^6\ {}^2\mathrm{S}_{1/2}$	3.507E+00	3.499E+00	3.099E+00	2.698E+00	2.305E+00	1.789E+00	1.399E+00	1.041E+00	6.621E-01	5.649E-01
$5p^4\ (^3\mathrm{P}_2)\ 6s\ ^2[2]_{5/2}$	4.434E+00	3.874E+00	2.976E+00	2.293E+00	1.676E+00	1.071E+00	7.676E-01	5.632E-01	3.957E-01	3.963E-01
$5p^4\ (^3\mathrm{P}_2)\ 6s\ ^2[2]_{3/2}$	2.099E+00	1.843E+00	1.561E+00	1.327E+00	1.082E+00	8.836E-01	9.347E-01	1.238E+00	1.959E+00	2.853E+00
$5p^4\ (^3\mathrm{P}_2)\ 5d\ ^2[2]_{5/2}$	3.021E+00	2.996E+00	2.745E+00	2.343E+00	1.879E+00	1.356E+00	1.051E+00	7.963E-01	5.177E-01	4.272E-01
$5p^4\ (^3\mathrm{P}_2)\ 5d\ ^2[3]_{7/2}$	3.652E+00	3.762E+00	3.474E+00	2.967E+00	2.367E+00	1.672E+00	1.263E+00	9.117E-01	5.332E-01	3.229E-01
$5p^4\ (^3\mathrm{P}_2)\ 5d\ ^2[2]_{3/2}$	1.780E+00	1.750E+00	1.579E+00	1.332E+00	1.056E+00	7.604E-01	6.004E-01	4.717E-01	3.280E-01	3.074E-01
$5p^4\ (^3\mathrm{P}_2)\ 5d\ ^2[1]_{1/2}$	1.070E+00	1.048E+00	8.821E-01	7.091E-01	5.414E-01	3.687E-01	2.759E-01	2.009E-01	1.214E-01	8.172E-02
$5p^4\ (^3\mathrm{P}_2)\ 5d\ ^2[4]_{9/2}$	2.172E+00	2.277E+00	2.151E+00	1.874E+00	1.522E+00	1.105E+00	8.550E-01	6.373E-01	3.941E-01	2.710E-01
$5p^4\ (^3\mathrm{P}_0)\ 6s\ ^2[0]_{1/2}$	7.767E-01	7.120E-01	5.984E-01	4.956E-01	4.042E-01	3.300E-01	3.133E-01	3.407E-01	4.440E-01	6.100E-01
$5p^4\ (^3\mathrm{P}_2)\ 5d\ ^2[4]_{7/2}$	2.191E+00	2.119E+00	1.854E+00	1.557E+00	1.240E+00	8.982E-01	7.190E-01	5.928E-01	4.687E-01	4.515E-01
$5p^4\ (^3\mathrm{P}_1)\ 6s\ ^2[1]_{3/2}$	1.009E+00	9.506E-01	8.113E-01	6.912E-01	5.874E-01	5.272E-01	5.806E-01	7.635E-01	1.185E+00	1.714E+00
$5p^4\ (^3\mathrm{P}_1)\ 5d\ ^2[1]_{1/2}$	1.902E+00	1.755E+00	1.498E+00	1.294E+00	1.112E+00	9.796E-01	9.736E-01	1.068E+00	1.330E+00	1.771E+00
$5p^4\ (^3\mathrm{P}_2)\ 5d\ ^2[1]_{3/2}$	1.587E+00	1.479E+00	1.291E+00	1.144E+00	1.031E+00	9.910E-01	1.037E+00	1.182E+00	1.522E+00	2.047E+00
$5p^4\ (^3\mathrm{P}_2)\ 5d\ ^2[0]_{1/2}$	4.422E-01	4.096E-01	3.533E-01	3.016E-01	2.515E-01	2.090E-01	1.953E-01	1.940E-01	2.082E-01	2.607E-01
$5p^4\ (^3\mathrm{P}_2)\ 5d\ ^2[3]_{5/2}$	1.645E-01	1.503E-01	1.403E-01	1.275E-01	1.093E-01	8.864E-02	7.754E-02	6.917E-02	6.295E-02	7.356E-02
$5p^4\ (^3\mathrm{P}_1)\ 6s\ ^2[1]_{1/2}$	3.136E-01	3.039E-01	2.950E-01	2.831E-01	2.596E-01	2.473E-01	2.844E-01	3.877E-01	6.224E-01	9.114E-01
$5p^4\ (^3\mathrm{P}_0)\ 5d\ ^2[2]_{3/2}$	6.770E-01	6.502E-01	5.869E-01	5.237E-01	4.510E-01	3.568E-01	2.915E-01	2.323E-01	1.653E-01	1.589E-01
$5p^4\ (^3\mathrm{P}_1)\ 5d\ ^2[1]_{3/2}$	1.240E+00	1.246E+00	1.199E+00	1.119E+00	1.028E+00	9.568E-01	9.715E-01	1.086E+00	1.380E+00	1.850E+00
$5p^4\ (^3\mathrm{P}_0)\ 5d\ ^2[2]_{5/2}$	8.796E-01	8.692E-01	8.255E-01	7.444E-01	6.278E-01	4.873E-01	4.200E-01	3.750E-01	3.372E-01	3.845E-01
$5p^4\ (^3\mathrm{P}_1)\ 5d\ ^2[3]_{7/2}$	4.356E-01	4.387E-01	3.925E-01	3.325E-01	2.659E-01	1.956E-01	1.614E-01	1.406E-01	1.236E-01	1.268E-01
$5p^4\ (^1\mathrm{D}_2)\ 6s\ ^2[2]_{5/2}$	9.216E-01	9.044E-01	8.299E-01	7.258E-01	5.993E-01	4.576E-01	4.060E-01	4.224E-01	5.415E-01	7.453E-01
$5p^4\ (^3\mathrm{P}_1)\ 5d\ ^2[2]_{3/2}$	5.726E-01	5.167E-01	4.227E-01	3.498E-01	2.826E-01	2.193E-01	1.918E-01	1.764E-01	1.711E-01	2.039E-01
$5p^4\ (^3\mathrm{P}_2)\ 6p\ ^2[2]^{\mathrm{o}}_{3/2}$	3.955E-01	3.888E-01	3.511E-01	3.121E-01	2.710E-01	2.348E-01	2.113E-01	1.780E-01	1.247E-01	1.040E-01
$5p^4\ (^3\mathrm{P}_2)\ 6p\ ^2[2]^{\mathrm{o}}_{5/2}$	5.542E-01	5.457E-01	4.831E-01	4.246E-01	3.633E-01	2.986E-01	2.536E-01	1.998E-01	1.276E-01	9.194E-02
$5p^4\ (^3\mathrm{P}_1)\ 5d\ ^2[2]_{5/2}$	6.332E-01	5.952E-01	5.363E-01	4.876E-01	4.415E-01	4.223E-01	4.617E-01	5.694E-01	7.979E-01	1.104E+00
$5p^4\ (^1\mathrm{D}_2)\ 6s\ ^2[2]_{3/2}$	5.082E-01	4.827E-01	4.295E-01	3.770E-01	3.168E-01	2.448E-01	2.037E-01	1.794E-01	1.790E-01	2.250E-01
$5p^4\ (^3\mathrm{P}_2)\ 6p\ ^2[3]^{\mathrm{o}}_{5/2}$	9.922E-01	9.448E-01	8.601E-01	7.933E-01	7.394E-01	7.069E-01	6.769E-01	6.281E-01	5.286E-01	5.081E-01
$5p^4\ (^3\mathrm{P}_2)\ 6p\ ^2[1]^{\mathrm{o}}_{1/2}$	8.938E-01	8.273E-01	7.390E-01	6.653E-01	5.852E-01	4.982E-01	4.310E-01	3.558E-01	2.554E-01	2.248E-01
$5p^4\ (^3\mathrm{P}_2)\ 6p\ ^2[3]^{\mathrm{o}}_{7/2}$	1.312E+00	1.249E+00	1.150E+00	1.094E+00	1.070E+00	1.148E+00	1.310E+00	1.647E+00	2.323E+00	2.954E+00
$5p^4\ (^3\mathrm{P}_1)\ 5d\ ^2[3]_{5/2}$	1.596E-01	1.643E-01	1.612E-01	1.464E-01	1.301E-01	1.240E-01	1.280E-01	1.302E-01	1.210E-01	1.321E-01
$5p^4\ (^1\mathrm{D}_2)\ 5d\ ^2[4]_{9/2}$	7.725E-01	7.994E-01	7.946E-01	7.352E-01	6.371E-01	5.223E-01	4.723E-01	4.423E-01	4.043E-01	4.164E-01
$5p^4\ (^1\mathrm{D}_2)\ 5d\ ^2[4]_{7/2}$	8.925E-01	8.386E-01	7.615E-01	6.866E-01	5.929E-01	4.687E-01	3.795E-01	2.867E-01	1.750E-01	1.216E-01
$5p^4\ (^3\mathrm{P}_2)\ 6p\ ^2[1]^{\mathrm{o}}_{3/2}$	6.404E-01	6.395E-01	6.391E-01	6.172E-01	6.257E-01	8.714E-01	1.226E+00	1.486E+00	1.466E+00	1.470E+00
$5p^4\ (^1\mathrm{D}_2)\ 5d\ ^2[3]_{5/2}$	6.678E-01	6.422E-01	6.063E-01	5.869E-01	5.944E-01	6.487E-01	7.122E-01	8.393E-01	1.130E+00	1.549E+00
$5p^4\ (^3\mathrm{P}_0)\ 6p\ ^2[1]^{\mathrm{o}}_{1/2}$	3.436E-01	3.333E-01	3.095E-01	2.751E-01	2.399E-01	2.190E-01	2.214E-01	2.352E-01	2.669E-01	3.127E-01
$5p^4\ (^1\mathrm{D}_2)\ 5d\ ^2[3]_{7/2}$	4.316E-01	4.384E-01	4.202E-01	3.737E-01	3.110E-01	2.422E-01	2.114E-01	1.886E-01	1.575E-01	1.529E-01
$5p^4\ (^3\mathrm{P}_1)\ 6p\ ^2[0]^{\mathrm{o}}_{1/2}$	2.408E-01	2.307E-01	2.061E-01	1.816E-01	1.580E-01	1.337E-01	1.148E-01	9.536E-02	7.337E-02	6.976E-02
$5p^4\ (^3\mathrm{P}_0)\ 6p\ ^2[1]^{\mathrm{o}}_{3/2}$	2.460E-01	2.339E-01	2.052E-01	1.809E-01	1.590E-01	1.383E-01	1.219E-01	1.019E-01	7.256E-02	6.236E-02

3.2. Differential Cross Sections

Differential cross sections (DCS) provide a sensitive probe of the angular distribution in collision dynamics and constitute essential input for modeling low-temperature plasmas[9]. In this work, DCS for electron impact excitation of Xe II were calculated within the DBSR-67 model at six incident electron energies between 20 and 30 eV. Results for selected fine-structure-resolved transitions from the ground state are presented in Figure 6. As no comparable data are currently available, the discussion below focuses on characterizing the features of the present results.

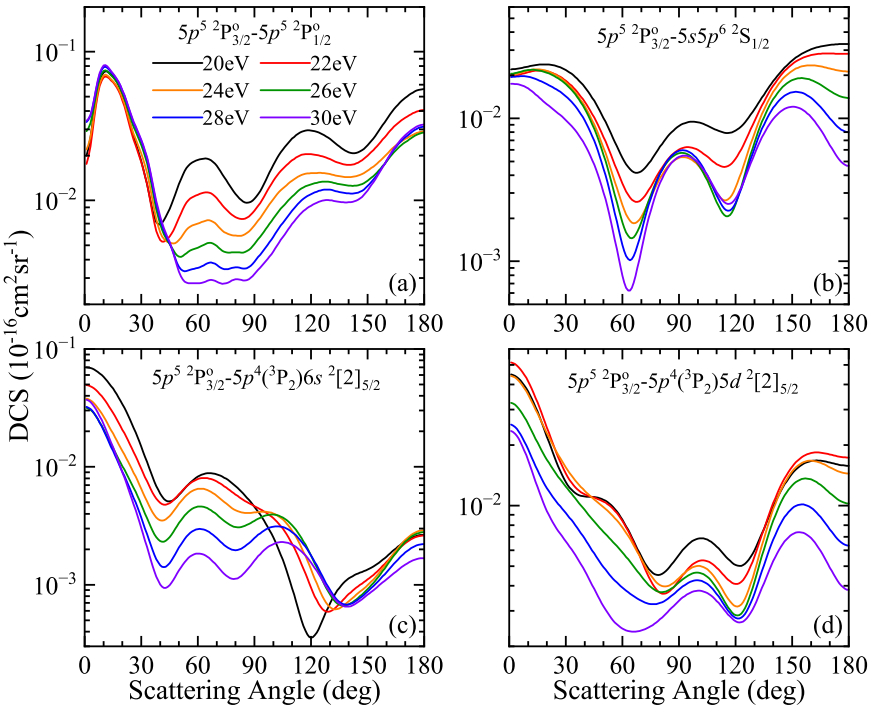


Figure 6: DCS as a function of the scattering angle of the electron impact excitation from the ground state $5p^5\ ^2P^o_{3/2}$ to four excited levels.

The DCS curves in Figure 6 exhibit pronounced angular dependence and systematic variations with incident energy, which reflects the changing balance between various interactions in the electron scattering processes. The curves in each panel reach comparatively large values and retain a broadly similar shape across the six incident energies at small scattering angles below 30 degrees. This pattern is consistent with small-angle scattering being dominated by the long-range Coulomb interaction between the projectile and the target, which varies smoothly with energy and therefore leaves the shape of the scattering amplitude largely unperturbed in this region. Toward larger angles, short-range exchange and correlation interactions, associated with closer collisions that more directly probe the ionic core, become increasingly important. These interactions drive the growing energy sensitivity common to every panel. As additional channels become energetically accessible, their mutual coupling reshapes the scattering amplitude. Additional minima or maxima appear in the curves of all four panels, strengthening or shifting sensitively within the present energy window.

Beyond the common pattern, each panel carries its own signature. For the dipole-forbidden gs-$5p^5\ ^2P^o_{1/2}$ transition in panel (a), the presence of a small-angle peak near 10 degrees illustrates the importance of intermediate-

coupling (jj-LS) mixing for this heavy, strongly spin-orbit coupled ion. Relativistic mixing among the $5p^5\ ^2\mathrm{P}^{\mathrm{o}}_{3/2}$ and $^2\mathrm{P}^{\mathrm{o}}_{1/2}$ fine-structure levels allows a small but non-zero effective dipole-type coupling to enter the scattering amplitude, superposed on the dominant exchange and correlation contributions that control the larger-angle behavior. Beyond 40 degrees, the curves diverge and their magnitudes decrease with increasing incident energy. Below 24 eV, two additional maxima emerge near 65 and 125 degrees. These features progressively weaken as the incident energy increases. The curves of the inner shell gs-$5s5p^6\ ^2\mathrm{S}_{1/2}$ excitation in panel (b) show a single broad maximum near 90 degrees flanked by valleys near 65 and 115 degrees, and the valley at 65 degrees is significantly deeper than that at 115 degrees. This possibly reflects the distinct orbital character of this $5s$-subshell transition. Panels (c) and (d) both show minima whose development is strongly energy-dependent. For the gs-$5p^4\ (^3\mathrm{P}_2)\ 6s\ ^2[2]_{5/2}$ transition in panel (c), the curves develop an additional minimum near 80 degrees that becomes distinct at 26 eV and above but diminishes at lower energy. The minimum with the largest scattering angle shifts and rises from about 120 degrees at 20 eV to about 140 degrees and coincides at 26 eV and above. For the gs-$5p^4\ (^3\mathrm{P}_2)\ 5d\ ^2[2]_{5/2}$ transition in panel (d), an additional plateau can be observed in the curves of 20 and 22 eV around 45 degrees, which leads to the intersection of the curves of 20, 22 and 24 eV. This feature diminishes at higher incident energies. The valley near 70 degrees broadens and shifts to smaller angles as the energy approaches 30 eV. These minima are characteristic interference features that arise when several partial waves of comparable magnitude but different parity contribute to the scattering amplitude. Their position and depth are therefore expected to be sensitive to the relative phases of the dominant partial waves, which in turn evolve rapidly with energy in the vicinity of the excitation threshold. Taken together, these results suggest that DCS shape in electron impact excitation of Xe II is governed by the angle-dependent competition between long-range and short-range interactions, with the resulting partial-wave interference pattern at backward angles further modulated by channel-coupling effects near threshold.

4. Conclusion

In the present work, we performed detailed theoretical calculations for the electron impact excitation of Xe II using the fully relativistic Dirac B-spline R-matrix (DBSR) method. Extensive results were obtained for electric dipole-allowed radiative parameters, integral and differential cross sections, as well as the corresponding Maxwellian-averaged effective collision strengths for transitions between the 67 low-lying fine-structure levels of the $5s^25p^5$, $5s5p^6$, $5p^46s$, $5p^45d$, $5p^46p$, and $5p^47s$ configurations. To capture the inherent complexity of this heavy ion target, the multi-electron Dirac-Coulomb Hamiltonian was employed, ensuring a comprehensive treatment of both valence and core-valence correlations alongside the relativistic effects. A key methodological advantage lies in the use of non-orthogonal orbital sets for constructing target wave functions and representing scattering functions. This flexibility permits the independent optimization of individual wave functions, thereby yielding a more accurate target description than what is usually possible with orthogonal orbital sets, in particular if the target states are to be used in a subsequent collision calculation. Building on the previous research of Wang et al.[21], we made a modest extension to the CI expansion of the target wavefunctions, to further improve the convergence and accuracy of the structure calculations. On this basis, we provided a full set of radiative parameters, including line strengths, transition probabilities, and oscillator strengths, for all 701 electric dipole-allowed transitions of the Xe II model. The oscillator

strengths were further classified according to the relative differences between their length-form and velocity-form values: about 80% of these relative differences lie within 25%. The theoretical oscillator strengths are also in good agreement with the available experimental data from NIST ASD[28] and other published measurements[5]. These results gave confidence in our target description of Xe II. The subsequent scattering calculations also show good convergence with respect to the target states and partial-wave expansions. Electron impact excitation cross sections for all 2211 transitions among the 67 levels of Xe II were provided in the present dataset, and those for transitions from the ground state are in good agreement with the existing RDW calculations[20]. The newly calculated differential cross sections and effective collision strengths were also given in the dataset together. In summary, this study provides systematic and consistent datasets for electron impact excitation of Xe II, thereby fulfilling the data requirements for spectroscopic analysis and kinetic modeling in plasma research.

Data availability statement

The data that support the findings of this study are openly available in Science Data Bank at https://doi.org/10.57760/sciencedb.31170. This statement should be given if some related data have been deposited in Science Data Bank.

Acknowledgment

We acknowledge the support of Key Laboratory of Space Metrology Technology, State Administration for Market Regulation on the research. This work was also supported by the Fundamental Research Funds for the Central Universities No. 2023FRFK06006 and the National Natural Science Foundation of China under Grant No. U22B2094.

References

[1] Goebel D M and Katz I 2008 *Fundamentals of electric propulsion: ion and hall thrusters* (Wiley)
[2] Boeuf J P 2017 *J. Appl. Phys.* **121** 011101
[3] Sutton G P and Biblarz O 2010 *Rocket propulsion elements* (John Wiley & Sons)
[4] Hill K W, Scott S D, Bell M *et al.* 1999 *Phys. Plasmas* **6** 877
[5] Yüce K, Castelli F and Hubrig S 2011 *Astron. & Astrophys.* **528** A37
[6] Di Rocco H O, Cruzado A and Marchiano P E 2015 *Astron. & Astrophys.* **581** A63
[7] Zhu X M, Chen W C, Li J *et al.* 2008 *J. Phys. D: Appl. Phys.* **42** 025203
[8] Zhu X M and Pu Y K 2010 *J. Phys. D: Appl. Phys.* **43** 403001
[9] Gangwar R K, Sharma L, Srivastava R *et al.* 2010 *Phys. Rev. A* **81**(5) 052707
[10] Jung R O, Boffard J B, Anderson L W *et al.* 2009 *Phys. Rev. A* **80**(6) 062708
[11] Zatsarinny O and Bartschat K 2010 *J. Phys. B: At. Mol. Opt. Phys.* **43** 074031
[12] Priti, Gangwar R K and Srivastava R 2019 *Plasma Sources Sci. Technol.* **28** 025003
[13] Gigosos M A, Mar S, Pérez C *et al.* 1994 *Phys. Rev. E* **49**(2) 1575
[14] Rocco H O D, Iriarte D I and Pomarico J A 2000 *Eur. Phys. J. D* **10** 19
[15] Zielińska S, Bratasz L and Dzierżęga K 2002 *Phys. Scr.* **66** 454
[16] Sayres S G, Hosler E R and Leone S R 2014 *J. Phys. Chem. A.* **118** 8614

[17] Fushitani M, Kawabe Y, Fujise H *et al.* 2021 *Phys. Rev. A* **104**(2) 023102

[18] Zhang S, Zhang F, Zhang D *et al.* 2024 *Chinese Physics B* **33** 033401

[19] Wei P, Huang C, Cheng X *et al.* 2024 *Chinese Physics B* **33** 043101

[20] Gupta S, Sharma L and Srivastava R 2018 *J. Quant. Spectrosc. Radiat. Transf.* **219** 7

[21] Wang Y, Wang Y F, Zhu X *et al.* 2019 *Plasma Sources Sci. Technol.* **28** 105004

[22] Zhu X M, Wang Y F, Wang Y *et al.* 2019 *Plasma Sources Sci. Technol.* **28** 105005

[23] Zhu X M, Wang Y F, Meng S F *et al.* 2023 *Plasma Sources Sci. Technol.* **32** 095019

[24] Zatsarinny O and Bartschat K 2008 *Phys. Rev. A* **77**(6) 062701

[25] Zatsarinny O 2006 *Comput. Phys. Commun.* **174** 273

[26] Jönsson P, He X, Froese Fischer C *et al.* 2007 *Journal reference: Comput. Phys. Commun* **177** 597

[27] Zatsarinny O and Froese Fischer C 2016 *Comput. Phys. Commun.* **202** 287

[28] https://physics.nist.gov/asd

[29] Froese Fischer C and Zatsarinny O 2009 *Comput. Phys. Commun.* **180** 879

[30] Visscher L and Dyall K 1997 *At. Data Nucl. Data Tables* **67** 207

[31] http://netlib.org/scalapack/

[32] Burke V and Noble C 1995 *Comput. Phys. Commun.* **85** 471

[33] Seaton M J 1987 *J. Phys. B: At. Mol. Opt. Phys.* **20** 6363

[34] Grum-Grzhimailo A 2003 *Comput. Phys. Commun.* **152** 101

[35] Chung H K, Braams B J, Bartschat K *et al.* 2016 *J. Phys. D: Appl. Phys.* **49** 363002